Dissecting Rate-Limiting Processes in Biomolecular Condensate Exchange Dynamics

Ross Kliegman,[1,*] Eli Kengmana,[2] Rebecca Schulman,[2,3,4] and Yaojun Zhang[1,5,*]

[1] *Department of Physics & Astronomy, Johns Hopkins University, Baltimore, Maryland 21218, USA*
[2] *Chemistry-Biology Interface Program, Johns Hopkins University, Baltimore, Maryland 21218, USA*
[3] *Department of Chemical & Biomolecular Engineering, Johns Hopkins University, Baltimore, Maryland 21218, USA*
[4] *Department of Computer Science, Johns Hopkins University, Baltimore, Maryland 21218, USA*
[5] *Department of Biophysics, Johns Hopkins University, Baltimore, Maryland 21218, USA*

(Dated: May 16, 2025)

An increasing number of biomolecules have been shown to phase-separate into biomolecular condensates — membraneless subcellular compartments capable of regulating distinct biochemical processes within living cells. The speed with which they exchange components with the cellular environment can influence how fast biochemical reactions occur inside condensates and how fast condensates respond to environmental changes, thereby directly impacting condensate function. While Fluorescence Recovery After Photobleaching (FRAP) experiments are routinely performed to measure this exchange timescale, it remains a challenge to distinguish the various physical processes limiting fluorescence recovery and identify each associated timescale. Here, we present a reaction-diffusion model for condensate exchange dynamics and show that such exchange can differ significantly from that of conventional liquid droplets due to the presence of a percolated molecular network, which gives rise to different mobility species in the dense phase. In this model, exchange can be limited by diffusion of either the high- or low-mobility species in the dense phase, diffusion in the dilute phase, or the attachment/detachment of molecules to/from the network at the surface or throughout the bulk of the condensate. Through a combination of analytic derivations and numerical simulations in each of these limits, we quantify the contributions of these distinct physical processes to the overall exchange timescale. Demonstrated on a biosynthetic DNA nanostar system, our model offers insight into the predominant physical mechanisms driving condensate material exchange and provides an experimentally testable scaling relationship between the exchange timescale and condensate size. Interestingly, we observe a newly predicted regime in which the exchange timescale scales nonquadratically with condensate size.

INTRODUCTION

Recent discoveries have found that living cells exploit a type of phase transition known as liquid-liquid phase separation for intracellular organization. This new paradigm challenges the traditional textbook view of the cell that organelles are mostly membrane-bound. Rather, subcellular structures can take the form of dynamic, liquid-like networks of molecules called "biomolecular condensates" [1, 2]. These condensates are dense assemblies of distinct proteins and nucleic acids that are driven by multivalent interactions to segregate out of the intracellular milieu. They enable functions vital for life, including gene regulation [3–5], signal transduction [6–8], and stress response [9–11], and when misregulated, they have been implicated in various diseases, most notably neurodegeneration [12–14] and cancer [15–18]. Understanding how condensates form and evolve over time in cells can deepen our physical understanding of emergent self-organization in biological systems and potentially inform human health.

The earliest measurements of condensate physical properties were made on *Caenorhabditis elegans* germ granules, or P granules, which were shown to be liquid-like — they constantly fuse with each other, flow under applied shear stresses, and undergo internal rearrangement [19]. Often essential for their biological functions, the liquid-like nature of condensates enables them to exchange materials with the surrounding dilute phase. For instance, metabolic condensates, such as purinosomes [20, 21], are enriched in enzymes, substrates, and other biomolecules involved in specific metabolic pathways [22]. Regulating metabolic activity in condensates requires not only that reactants can partition into them, but also that products can later escape. However, with viscosities orders of magnitude larger than conventional oil droplets [23], condensates are thought to experience slow internal diffusion, limiting the exchange dynamics. More broadly, the speed of material exchange can influence the response of condensates to environmental changes, as well as the number, size, and spatial distribution of condensates via Ostwald ripening [24, 25]. Collectively, these effects can impact condensate function, motivating a need for tools to accurately measure and interpret the exchange dynamics.

The timescales of molecular exchange are commonly measured with an experimental technique known as Fluorescence Recovery After Photobleaching (FRAP) [26–29]. In a typical FRAP experiment, fluorescently labeled molecules are photobleached within a region of interest (ROI) upon irradiation with a high-intensity laser. The fluorescence intensity in the ROI then recovers over time due to molecular exchange with the surroundings until

constant intensity is eventually restored. Photobleaching can be performed on a subregion within a droplet, known as partial FRAP, or on an entire droplet, known as full FRAP. Exchange dynamics have been studied in a range of experimental condensate systems [6, 10, 30–33], and complementary theories were developed to extract meaningful physical quantities from measured fluorescence recovery curves [34–37]. Notably, all of these studies made an assumption that the exchange dynamics were limited by molecular diffusion. However, recent studies suggest that condensate material exchange can also be limited by other physical processes due to the complexity of molecular interactions [38–42], e.g., interface resistance [41, 42].

The exchange dynamics of condensates are ultimately determined by the constituent biomolecules and their microscopic structures and interactions. While phase-separating molecules often exhibit a complex set of interactions, they generally conform to a "sticker-spacer" architecture [43, 44], where "stickers" represent residues, nucleotide segments, or larger folded domains capable of forming reversible physical cross-links that drive phase separation, and "spacers" exclude volume and connect the stickers to form polymers. In the sticker-spacer framework, it follows that phase-separating molecules often form dynamically restructuring networks that go beyond traditional liquid-liquid phase separation (Fig. 1a), sometimes referred to as "phase separation coupled to percolation" [45, 46]. In the modified physical picture (Fig. 1b), attachment/detachment of molecules to/from the percolated network intuitively gives rise to different mobility populations within the condensate for the same type of molecule. The low-mobility population (referred to as "species 1") represents molecules bound to the network, and the high-mobility population (referred to as "species 2") represents freely diffusing molecules detached from the network. Indeed, multiple mobility populations have been reported in the dense phase of an *in vitro* reconstituted postsynaptic density system [47] as well as single-component A1-LCD condensates [48]. However, a theory to interpret such experimental results has been missing. Here, we present a model that accounts for a condensate's molecular network and discuss some of its implications for the exchange timescale.

RESULTS

A reaction-diffusion model for condensate exchange dynamics

To explore how the percolated network and the presence of two mobility species impact the condensate exchange timescale, we first develop a reaction-diffusion model for a phase-separated system at equilibrium. Assuming a spherical condensate, we describe the recovery dynamics of a bleached condensate (equivalent to the exchange dynamics) by the following coupled reaction-diffusion equations:

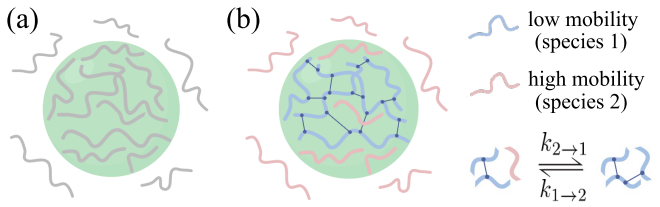

FIG. 1. Schematics of a condensate in (a) the conventional model, which assumes uniform molecular mobility inside and outside the condensate (depicted in grey), and (b) our proposed model, in which binding kinetics with the molecular network can give rise to multiple mobilities for the same molecule inside the condensate. Connected blue molecules are bound to the network, whereas individual pink molecules are freely diffusing. By attaching and detaching, the two mobility species can convert between one another with rates $k_{2\to1}$ and $k_{1\to2}$, respectively.

$$\frac{\partial c_1}{\partial t} = \nabla\cdot\left[D_1\left(\nabla c_1 - c_1\frac{\nabla c_1^{\mathrm{eq}}}{c_1^{\mathrm{eq}}}\right)\right] + k\left(c_1^{\mathrm{eq}}c_2 - c_2^{\mathrm{eq}}c_1\right), \quad (1)$$

$$\frac{\partial c_2}{\partial t} = \nabla\cdot\left[D_2\left(\nabla c_2 - c_2\frac{\nabla c_2^{\mathrm{eq}}}{c_2^{\mathrm{eq}}}\right)\right] - k\left(c_1^{\mathrm{eq}}c_2 - c_2^{\mathrm{eq}}c_1\right), \quad (2)$$

where $c_1(r,t)$ and $c_2(r,t)$ are the bleached concentrations of species 1 and 2, respectively, $D_1(r)$ and $D_2(r)$ are their position-dependent diffusion coefficients, $c_1^{\mathrm{eq}}(r)$ and $c_2^{\mathrm{eq}}(r)$ are their equilibrium concentration profiles, and k is a parameter that encodes how fast molecules convert between species. The coordinate r is the distance from the center of the condensate, and t denotes the time.

In Eqs. (1) and (2), the first terms on the right represent conventional Fickian diffusion in a concentration gradient, and the second terms represent excess chemical potentials that drive molecules towards nonuniform equilibrium concentration profiles. The third and fourth terms account for mobility switching due to binding/unbinding with the network. Molecules can attach to the percolated network and lower their mobility with a rate $k_{2\to1}(r)$, and detach from the network and regain higher mobility with a rate $k_{1\to2}(r)$. Detailed balance requires that the fluxes of association ($c_2k_{2\to1}$) and dissociation ($c_1k_{1\to2}$) are equal at equilibrium, which allows us to characterize these rates in terms of a single parameter, $k(r) \equiv k_{2\to1}(r)/c_1^{\mathrm{eq}}(r) = k_{1\to2}(r)/c_2^{\mathrm{eq}}(r)$. For simplicity, we assume k to be a constant, independent of the location of the molecule. The system reaches equilibrium when $c_1(r,t)/c_1^{\mathrm{eq}}(r) = c_2(r,t)/c_2^{\mathrm{eq}}(r) = f_b$, where the constant f_b is the fraction of total molecules that are bleached.

Analogous to a FRAP experiment, we set the initial

condition to be

$$c_i(r,0) = \begin{cases} c_i^{\mathrm{eq}}(r), & r \le R; \\ 0, & r > R \end{cases} \tag{3}$$

for a fully bleached droplet, where $i = 1, 2$, and R is the droplet radius. We impose no-flux boundary conditions to conserve total particle number in the system:

$$\left.\frac{\partial c_i(r,t)}{\partial r}\right|_{r=0} = \left.\frac{\partial c_i(r,t)}{\partial r}\right|_{r=+\infty} = 0. \tag{4}$$

Upon solving for $c_1(r,t)$ and $c_2(r,t)$, we can obtain a normalized brightness curve $I(t)$ for the fraction of molecules inside the droplet that are unbleached at a time t:

$$I(t) = 1 - \frac{\int_0^R \left[c_1(r,t) + c_2(r,t)\right] r^2 dr}{\int_0^R \left[c_1^{\mathrm{eq}}(r) + c_2^{\mathrm{eq}}(r)\right] r^2 dr}. \tag{5}$$

Finally, the characteristic timescale τ of the exchange dynamics is identified by fitting $I(t)$ to an exponential function of the form $1 - e^{-t/\tau}$.

Quantifying the timescales of rate-limiting processes

Analytical derivations

A proxy for condensate material exchange, fluorescence recovery in a bleached droplet is a multi-step process involving dilute-phase diffusion, network attachment/detachment, and dense-phase diffusion. We outline the rate-limiting steps of FRAP recovery in Fig. 2. First, an unbleached molecule must diffuse through the dilute phase to reach the droplet surface. In the limit of low dilute-phase concentration, we derive the dilute-phase diffusion timescale τ_{dil} shown in Eq. (6a). Next, in the limit of low dense-phase concentration of species 2, the unbleached molecule is more likely to enter the droplet by attaching to the network at the droplet interface and subsequently diffusing into the bulk dense phase as species 1. In this case, if interfacial attachment/detachment is rate-limiting, we derive the interface-limited timescale τ_{int} shown in Eq. (6b), whereas if dense-phase diffusion of species 1 is rate-limiting, we derive the timescale $\tau_{1,\mathrm{den}}$ shown in Eq. (6c). Finally, for sufficiently high dense-phase concentration of species 2, the unbleached molecule is more likely to enter the droplet by passing through the pores of the network and diffusing around the dense phase as species 2, which then attaches to and detaches from the network throughout the bulk of the droplet. In this case, if dense-phase diffusion of species 2 is rate-limiting, we derive the timescale $\tau_{2,\mathrm{den}}$ shown in Eq. (6d), whereas if attachment/detachment throughout the bulk of the droplet is rate-limiting, we derive the conversion-limited timescale τ_{con} shown in Eq. (6e). Detailed derivations of each timescale are provided in the Supplemental Material [49].

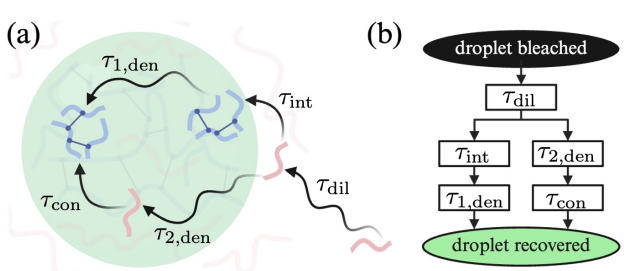

FIG. 2. Schematic (a) and flowchart (b) of rate-limiting processes in the exchange dynamics of biomolecular condensates. In order for fluorescence to recover in a bleached droplet, an unbleached molecule first has to diffuse in the dilute phase with a timescale τ_{dil} until it encounters the droplet, and then either attach to the network at the surface with a timescale τ_{int} and diffuse into the droplet with a timescale $\tau_{1,\mathrm{den}}$, or diffuse through the network mesh inside the droplet with a timescale $\tau_{2,\mathrm{den}}$ and subsequently attach to the network within the droplet bulk with a timescale τ_{con}.

$$\tau_{\mathrm{dil}} = \frac{R^2 c_{1,\mathrm{den}}}{3 D_{2,\mathrm{dil}} c_{2,\mathrm{dil}}}, \tag{6a}$$

$$\tau_{\mathrm{int}} = \frac{R}{3 k c_{2,\mathrm{dil}} \delta_{\mathrm{eff}}}, \tag{6b}$$

$$\tau_{1,\mathrm{den}} = \frac{R^2}{\pi^2 D_{1,\mathrm{den}}}, \tag{6c}$$

$$\tau_{2,\mathrm{den}} = \frac{R^2 c_{1,\mathrm{den}}}{\pi^2 D_{2,\mathrm{den}} c_{2,\mathrm{den}}}, \tag{6d}$$

$$\tau_{\mathrm{con}} = \frac{1}{k c_{2,\mathrm{den}}}. \tag{6e}$$

$D_{1,\mathrm{den}}$ and $D_{2,\mathrm{den}}$ are the dense-phase diffusion coefficients of species 1 and 2, respectively, $c_{1,\mathrm{den}}$ and $c_{2,\mathrm{den}}$ are the dense-phase equilibrium concentrations of species 1 and 2, respectively, $D_{2,\mathrm{dil}}$ is the dilute-phase diffusion coefficient of species 2, $c_{2,\mathrm{dil}}$ is the dilute-phase equilibrium concentration of species 2, and δ_{eff} is the effective width of the droplet interface. We note that $c_{1,\mathrm{dil}} = 0$ as there is no percolated network in the dilute phase. The above derivations also assume $c_{2,\mathrm{den}} \ll c_{1,\mathrm{den}}$ as species 1 is energetically favored and therefore more abundant.

Each physical process has a distinct timescale that scales with droplet size differently. Specifically, the diffusion-limited processes in both dense and dilute phases are associated with timescales that naturally scale as R^2/D [Eqs. (6a), (6c), and (6d)]. The factors $c_{1,\mathrm{den}}/c_{2,\mathrm{dil}}$ and $c_{1,\mathrm{den}}/c_{2,\mathrm{den}}$ in Eqs. (6a) and (6d) account for replacing bleached molecules of concentration $c_{1,\mathrm{den}}$ with unbleached molecules of concentrations $c_{2,\mathrm{dil}}$ and $c_{2,\mathrm{den}}$, respectively. The interfacial timescale [Eq. (6b)] accounts for exchange of a volume of molecules ($\sim R^3$) over a surface ($\sim R^2$) and is therefore linear in

R. Lastly, the conversion-limited timescale [Eq. (6e)] is independent of R, which arises due to rate-limiting detachment of bleached molecules throughout the bulk of the dense phase, i.e., the lifetime of a molecule in the network [given by $1/k_{1\to 2} = 1/(kc_{2,\mathrm{den}})$]. Once detached, these molecules can quickly escape the droplet, allowing unbleached molecules to attach to the network.

Putting together the rate-limiting steps, we propose the following expression for the overall timescale of fluorescence recovery:

$$\tau = \tau_{\mathrm{dil}} + \left[(\tau_{\mathrm{int}} + \tau_{1,\mathrm{den}})^{-1} + (\tau_{2,\mathrm{den}} + \tau_{\mathrm{con}})^{-1} \right]^{-1}, \quad (7)$$

where following diffusion in the dilute phase, two competing modes of recovery occur in parallel, each a sequence of two steps (Fig. 2b). It is worth noting that by setting $c_{2,\mathrm{den}} = 0$ in Eq. (7), i.e., assuming a single mobility species inside the droplet, we recover results of our previous study [41]. In particular, Eq. (6b) arises due to the "interface resistance" of the droplet, which was previously modeled with a phenomenological parameter κ, but now acquires a clear physical meaning: τ_{int} is governed by the molecular attachment/detachment at the droplet interface. For $c_{2,\mathrm{den}} > 0$, the emergence of a new pathway in Fig. 2 leads to two previously unrecognized terms in the recovery time [Eq. (7)], resulting in a complex dependence of τ on the droplet radius R. We demonstrate this complex dependence via numerical simulations and FRAP experiments on DNA nanostar droplets below.

Numerical simulations

In the previous section, we derived the timescale of fluorescence recovery by analytically solving the reaction-diffusion system described by Eqs. (1-5) in various limits. Here, we numerically verify these timescales and visualize the different FRAP signatures in each rate-limiting case. Specifically, we first specify the functional forms of equilibrium concentrations and diffusion coefficients with sharp but smooth transitions at the droplet interface ($r = R$) over a finite width $\sim l$:

$$c_i^{\mathrm{eq}}(r) = \frac{c_{i,\mathrm{dil}} - c_{i,\mathrm{den}}}{2} \tanh\left(\frac{r-R}{l}\right) + \frac{c_{i,\mathrm{dil}} + c_{i,\mathrm{den}}}{2},$$
$$D_i(r) = \frac{D_{i,\mathrm{dil}} - D_{i,\mathrm{den}}}{2} \tanh\left(\frac{r-R}{l}\right) + \frac{D_{i,\mathrm{dil}} + D_{i,\mathrm{den}}}{2},$$

which are consistent with equilibrium solutions of the Cahn-Hilliard equation [50]. The initial and boundary conditions are given by Eqs. (3) and (4), respectively, except that the boundary at $r = +\infty$ is replaced by $r = r_{\max}$ for the finite size of the system. We then solve Eqs. (1) and (2) numerically under spherical symmetry using the *pdepe* function in MATLAB, which employs finite-difference spatial discretization with a variable-step, variable-order solver for time integration [51]. The numerical solutions for $c_1(r,t)$ and $c_2(r,t)$ are used to compute a brightness curve in accordance with Eq. (5), which is subsequently fitted to extract the recovery timescale.

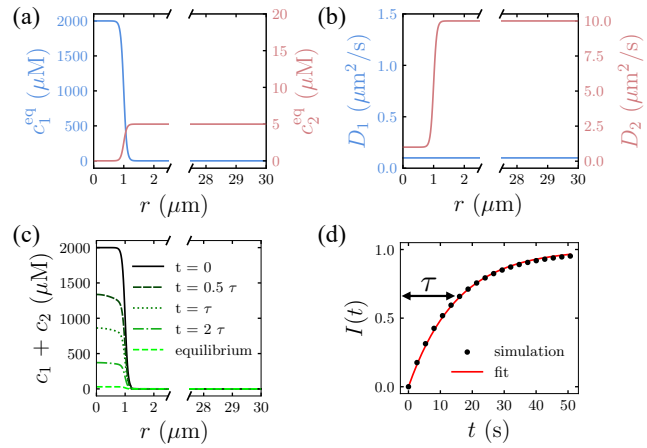

FIG. 3. Representative simulation in a dilute-phase diffusion-limited scenario (parameters from top row in Table I). (a) Equilibrium concentration profiles and (b) diffusivity profiles for species 1 and 2. (c) Simulated radial concentration profiles of the bleached molecules for a few illustrative times. (d) Simulated brightness curve with exponential fit using nonlinear least squares. Simulations were performed with radial step size $dr = 20\,\mathrm{nm}$ over a system size of $r_{\max} = 30\,\mu\mathrm{m}$ for 1000 timepoints (the solver dynamically selects both the timestep and formula).

We show an example where the FRAP recovery is limited by dilute-phase diffusion in Fig. 3. Guided by Eq. (7), we choose physiological parameters of condensate systems [23, 52, 53] that lead to $\tau \approx \tau_{\mathrm{dil}}$ (Table I). The numerically extracted relaxation time $\tau = 15.1\,\mathrm{s}$ of an $R = 1\,\mu\mathrm{m}$ droplet is indeed close to the theory prediction of $\tau_{\mathrm{dil}} = 13.3\,\mathrm{s}$. We repeat a similar procedure for various parameter sets in which the timescale of fluorescence recovery is limited by interfacial attachment/detachment, dense-phase diffusion of the low-mobility species, dense-phase diffusion of the high-mobility species, and attachment/detachment throughout the bulk of the condensate, totaling five cases. Simulated spatial fluorescence recovery profiles for each of these cases are shown in Fig. 4 with parameters listed in Table I. The two cases of dense-phase diffusion-limited recovery (rows c and d) can readily be distinguished by the pronounced gradient present due to unbleached molecules gradually diffusing into the condensate and bleached ones diffusing out, whereas the remaining three cases all display a uniform recovery. Details of the numerical implementation and fitting are provided in the Supplemental Material [49].

Based on Eq. (6), condensate recovery timescales are expected to follow different scaling laws in different

TABLE I. Parameter choice for numerical simulations of five rate-limiting cases.

Case	$c_{1,\mathrm{den}}$ (μM)	$c_{1,\mathrm{dil}}$ (μM)	$c_{2,\mathrm{den}}$ (μM)	$c_{2,\mathrm{dil}}$ (μM)	$D_{1,\mathrm{den}}$ ($\mu\mathrm{m}^2$/s)	$D_{1,\mathrm{dil}}$ ($\mu\mathrm{m}^2$/s)	$D_{2,\mathrm{den}}$ ($\mu\mathrm{m}^2$/s)	$D_{2,\mathrm{dil}}$ ($\mu\mathrm{m}^2$/s)	l (μm)	k ($\mu\mathrm{M}^{-1}\mathrm{s}^{-1}$)
$\tau \approx \tau_{\mathrm{dil}}$	2000	0	0	5	0.1	0.1	1	10	0.1	1
$\tau \approx \tau_{\mathrm{int}}$	1000	0	0	10	0.02	0.02	1	50	0.1	0.005
$\tau \approx \tau_{1,\mathrm{den}}$	1000	0	0	10	0.02	0.02	1	50	0.1	1
$\tau \approx \tau_{2,\mathrm{den}}$	1995	0	5	10	5×10^{-5}	5×10^{-5}	0.1	50	0.01	0.005
$\tau \approx \tau_{\mathrm{con}}$	980	0	20	10	0.02	0.02	1	50	0.05	1×10^{-4}

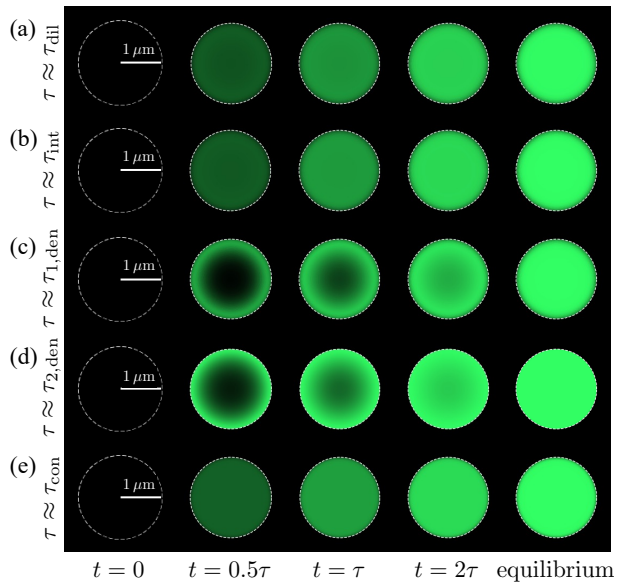

FIG. 4. Simulated FRAP recovery profiles when fluorescence recovery is limited by (a) dilute-phase diffusion, (b) interfacial attachment/detachment, (c) dense-phase diffusion of species 1, (d) dense-phase diffusion of species 2, and (e) attachment/detachment throughout the bulk of the condensate. Green indicates fluorescent molecules and black indicates bleached molecules. Simulations were performed with radial step sizes 1/5 of the interface width l, and the system size was $r_{\max} = 30\,\mu$m. 1000 timepoints were recorded over 4τ-long runtimes.

rate-limiting cases. As shown in Fig. 5, the different timescales indeed scale differently with droplet size *in silico* as well. When diffusive processes are rate-limiting, the scaling law is quadratic; when the interfacial flux is rate-limiting, the scaling law is linear; and when the network attachment/detachment throughout the droplet is rate-limiting, the scaling law is independent of droplet size.

Application to a DNA nanostar system

Finally, we sought to employ our theory in an experimental system composed of DNA nanostars — a model system for investigating biomolecular condensation. Thanks to advances in artificial DNA synthesis techniques, DNA nanostars offer highly programmable interactions: binding specificity and affinity can be tuned via the sequence and length of single-stranded overhangs, and valence via the number of arms. These features collectively enable a diverse range of phase behaviors [54–57]. Our DNA nanostars are composed of three arms of double-stranded DNA, each with a short tail of single-stranded DNA known as a "sticky end" due to its propensity to Watson-Crick base-pair with complementary strands (Fig. 6a). The sticky ends make these nanostars readily phase-separable, and micron-sized droplets can be seen with confocal microscopy. Details about sequences and sample preparation are given in the Supplemental Material [49].

DNA nanostars form porous networks inside their condensates, with the mesh size determined by the engineered arm length and valence [59, 60]. This property makes them a prime system in which to observe the new mode of recovery discussed above: nearby molecules may penetrate the droplet surface and diffuse freely within the droplet before attaching to the network. If this were the dominant recovery mechanism, we would expect to observe conversion-limited recovery for small droplets, transitioning to diffusion-limited recovery for large droplets. Upon performing FRAP on nanostar droplets of varying sizes (Fig. 6b), we noticed that the recovery curves and hence the recovery timescales were nearly identical for droplets of small sizes ($R \lesssim 1.5\,\mu$m), despite spanning nearly a twofold size range (Fig. 6c and 6d). This observation aligns with the scaling behavior of conversion-limited recovery. If the recovery of these droplets were diffusion-limited, whether by dilute-phase diffusion, species 1 dense-phase diffusion, or species 2 dense-phase diffusion, we would expect nearly a fourfold difference in exchange timescale. For larger droplets, we see a quadratic scaling that plateaus at the conversion-limited timescale (Fig. 6d). Upon fitting the data with the shifted quadratic function $\tau = a + bR^2$, we find the constants a and b are well-constrained: $a = 145.0 \pm 5.6$ s and $b = 14.1 \pm 0.7\,\mu\mathrm{m}^{-2}$s.

As suggested by our theory, the plateau regime arises because the recovery is conversion-limited, i.e., $\tau_{\mathrm{con}} = 1/(kc_{2,\mathrm{den}}) = a$. Nanostar droplets are porous, with a measured pore size comparable to the arm length. It has been reported that the partition coefficient for 70

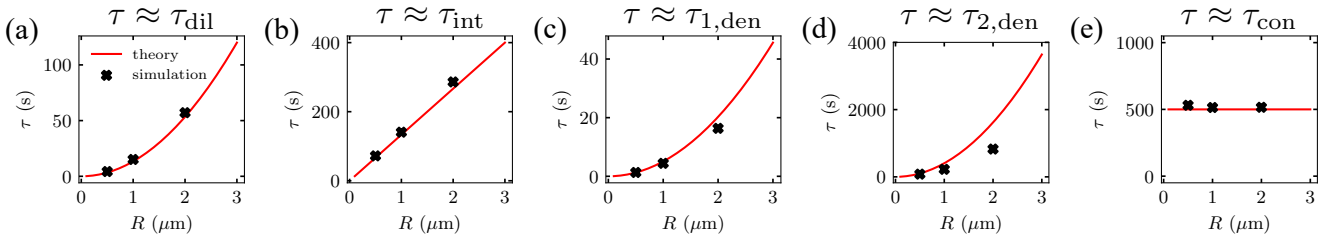

FIG. 5. Theoretical and simulated scaling laws show good agreement in each rate-limiting case: (a) dilute-phase diffusion-limited timescale scales with R^2, (b) interface-limited timescale scales with R, (c) dense-phase diffusion-limited timescale (species 1) scales with R^2, (d) dense-phase diffusion-limited timescale (species 2) scales with R^2, and (e) conversion-limited timescale is independent of R. Red curves: theoretical predictions from Eq. (6) using parameters from Table I; black crosses: simulation results for droplets of radii $R = 0.5\,\mu$m, $1\,\mu$m, and $2\,\mu$m.

kDa dextran (hydrodynamic radius 6 nm) is about 0.3 – 0.6 in such systems [59, 60]. Given that our nanostars have a hydrodynamic radius (5 – 7 nm) similar to that of dextran, we expect the unbound species of nanostars to partition in these nanostar droplets to a similar extent as the dextran. Assuming a partition coefficient of 0.5 and dilute-phase concentration of $1\,\mu$M, $c_{2,\rm den} \approx 0.5\,c_{2,\rm dil} \approx 0.5\,\mu$M, and the rate of nanostar attachment inside the condensate can be estimated as $k = 1/(ac_{2,\rm den}) \approx 0.014\,\mu{\rm M}^{-1}{\rm s}^{-1}$. This rate appears to be much lower than the reported on-rate for nanostars in dilute solution, which ranges from 0.1 to $1\,\mu{\rm M}^{-1}{\rm s}^{-1}$ [61]. The discrepancy likely arises because we have modeled the attachment flux as $kc_1^{\rm eq}c_2$ in Eq. (1), implicitly assuming that every species 1 nanostar in the percolated network can bind to freely diffusing species 2 nanostars. However, many nanostars in the network may already be in a fully bound state or spatially occluded and thus unavailable for binding, leading to a smaller apparent k. If we take these numbers seriously, this would suggest that about 90% of nanostars are not available for binding in the droplet.

Beyond the plateau regime, comparing the interface-limited timescale with the conversion-limited timescale gives the relation $\tau_{\rm int} = \tau_{\rm con}Rc_{2,\rm den}/(3\delta_{\rm eff}c_{2,\rm dil})$. Also, nanostar condensates have a surface tension around 1μN/m [56], which corresponds to an effective interface width $\delta_{\rm eff} \approx 30$ nm. Therefore, a droplet of radius R (in μm) would have an interface-limited timescale $\tau_{\rm int} \approx 800R$ s. Since this is much longer than the recovery times measured experimentally, we argue that the conventional pathway of attaching at the droplet interface followed by diffusion through the network is not the favored mode of recovery for the nanostar droplets studied here. This leads to a reduced expression for the overall relaxation time from Eq. (7): $\tau = \tau_{\rm dil} + \tau_{2,\rm den} + \tau_{\rm con}$. While $\tau_{\rm con} = a$ sets the plateau value, both $\tau_{\rm dil}$ and $\tau_{2,\rm den}$ scale with R^2 and can contribute to the prefactor $b = c_{1,\rm den}/(3D_{2,\rm dil}c_{2,\rm dil}) + c_{1,\rm den}/(\pi^2 D_{2,\rm den}c_{2,\rm den})$. Taking $c_{1,\rm den} = 200\,\mu$M, $c_{2,\rm dil} = 1\,\mu$M, $c_{2,\rm den} = 0.5\,\mu$M, and $D_{2,\rm dil} = 20\,\mu{\rm m}^2/{\rm s}$ (from the Stokes-Einstein relation) [58, 62], we estimate $D_{2,\rm den} \approx 4\,\mu{\rm m}^2/{\rm s}$.

DISCUSSION

A hallmark of biomolecular condensates is their dynamic exchange of materials with their surroundings, a feature often crucial to their function. In this work, we developed a novel reaction-diffusion model to describe condensate exchange dynamics and explored how such dynamics can deviate from those of conventional liquid droplets due to the formation of a percolated network in the condensate. We found that in the presence of two mobility states, material exchange can be accelerated via a new pathway in which molecules pass through the pores of the meshwork and attach/detach directly in the condensate interior. Notably, this pathway leads to a new regime where the exchange timescale becomes independent of condensate size, a prediction we confirmed using FRAP experiments on DNA nanostar condensates.

In this study, we focused on the exchange dynamics of *in vitro* single-component condensates and approximated a condensate as a two-state system at equilibrium. Molecules inside biological condensates, even in single-component systems, are likely to exhibit a broad range of mobilities due to the complexity of underlying interactions [47, 48]. A natural next step would be to incorporate more mobility states into the model. Nevertheless, a concise two-state model can capture the essential physical principles underlying condensate exchange dynamics while remaining analytically tractable.

The developed reaction-diffusion model can also be readily extended to describe multi-component systems. Condensates in living cells are complex assemblies of distinct proteins and nucleic acids, which generally employ a scaffold-client framework [45, 46]. While our model focused on the exchange dynamics of scaffold molecules, the same mathematical framework applies to client dynamics, where client molecules can bind (low mobil-

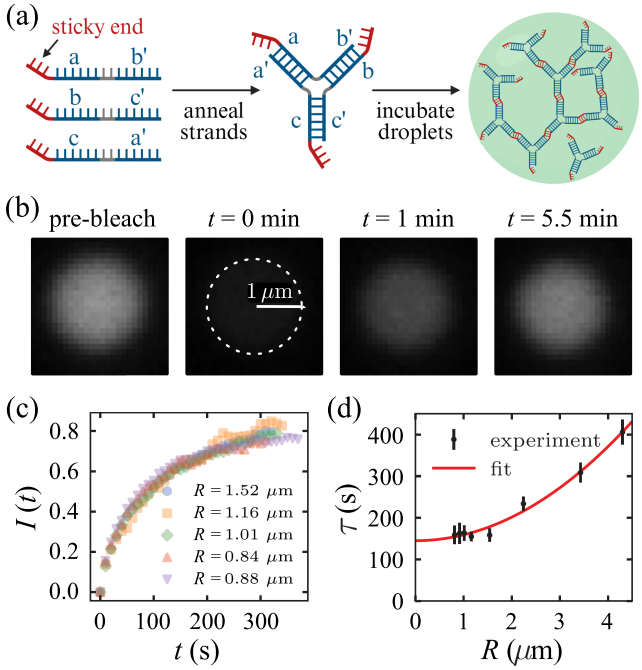

FIG. 6. Experimental characterization of exchange dynamics in DNA nanostar condensates. (a) Nanostar schematic. The Y-shaped nanostar has 16-bp double-stranded arms shown in blue, sticky ends with the palindromic sequence 5'-GCTAGC-3' in red, and non-complementary linkers with the sequence 5'-TT-3' in gray that confer angular flexibility between arms. The nanostars were first annealed in a low-salt solution, then added to a higher salt solution at 37 °C to incubate condensates, following the same protocol as in [58]. (b) Representative snapshots from a FRAP experiment of an $R = 1\,\mu$m nanostar droplet. (c) FRAP recovery curves for droplets of small sizes ($R \lesssim 1.5\,\mu$m). (d) Exchange timescale versus droplet radius for all droplets, fitted with a shifted quadratic function of the form $\tau = a + bR^2$, where $a = 145.0 \pm 5.6$ s and $b = 14.1 \pm 0.7\,\mu\text{m}^{-2}$s. Error bars are defined at 3σ.

ity)/unbind (high mobility) to/from an equilibrated scaffold network. The model can also be used to predict the dynamics of condensates in the cell nucleus, where molecules diffusing within the condensate are also capable of binding to/unbinding from DNA [63, 64].

The newly discovered pathway involves molecules passing through the pores of the meshwork and attaching/detaching directly within the condensate. In which systems, and for which molecules, would this pathway be favored and experimentally measurable? Because diffusion within the connected network for bound molecules is generally much slower than for unbound molecules, the essential requirement for this pathway to dominate is that the mesh size of the percolated network be comparable or larger than the size of the molecule of interest, ensuring a sufficiently high concentration of high-mobility species. It has been reported that the mesh size (or correlation length) for *in vitro* reconstituted condensates of purified LAF-1 protein is about 5 nm [65], while for reconstituted coacervates composed of two oppositely charged intrinsically disordered proteins, histone H1 and prothymosin-α, it is about 3 nm [66]. More generally, we established a quantitative relationship between mesh size and concentration in a recent work, which suggests that condensates at physiologically relevant concentrations of 100 – 400 mg/ml exhibit mesh sizes ranging from 8 to 3 nm [67]. Since protein sizes span the reported mesh size range, we expect the new pathway to be relevant to the exchange dynamics of many condensate systems, especially for condensates of low scaffold molecule concentrations and for clients of small sizes.

Fascinating soft matter systems in their own right, biomolecular condensates are also increasingly implicated in cellular physiology and disease [68, 69]. We hope that our work will motivate further theoretical and experimental investigations into the complex dynamics in multicomponent, multi-state condensates, shedding light on their functional roles and paving the way for applications in condensate bioengineering.

ACKNOWLEDGEMENTS

R.K. and Y.Z. were supported by a startup fund at Johns Hopkins University. E.K. acknowledges support from Sloan Foundation grant 138412 to R.S. and NIH grant T32GM080189. R.S. acknowledges support from Sloan Foundation grant 138412, DOE BES award DE-SC0010426 and NSF FET-2107246, ONR N00014-23-1-2868, and Kent Gordon Croft Investment Management Faculty Scholar fund.

* Contact authors: rkliegm1@jhu.edu (R.K.); yaojunz@jhu.edu (Y.Z.)

[1] S. F. Banani, H. O. Lee, A. A. Hyman, and M. K. Rosen, Biomolecular condensates: organizers of cellular biochemistry, Nat. Rev. Mol. Cell Biol. **18**, 285 (2017).

[2] Y. Shin and C. P. Brangwynne, Liquid phase condensation in cell physiology and disease, Science **357**, eaaf4382 (2017).

[3] I. I. Cisse, I. Izeddin, S. Z. Causse, L. Boudarene, A. Senecal, L. Muresan, C. Dugast-Darzacq, B. Hajj, M. Dahan, and X. Darzacq, Real-time dynamics of RNA polymerase II clustering in live human cells, Science **341**, 664 (2013).

[4] B. R. Sabari, A. Dall'Agnese, A. Boija, I. A. Klein, E. L. Coffey, K. Shrinivas, B. J. Abraham, N. M. Hannett, A. V. Zamudio, J. C. Manteiga, C. H. Li, Y. E. Guo, D. S. Day, J. Schuijers, E. Vasile, S. Malik, D. Hnisz, T. I. Lee, I. I. Cisse, R. G. Roeder, P. A. Sharp, A. K. Chakraborty, and R. A. Young, Coactivator condensation at super-enhancers links phase separation and gene control, Science **361**, eaar3958 (2018).

[5] T. Hirose, K. Ninomiya, S. Nakagawa, and T. Yamazaki, A guide to membraneless organelles and their various

roles in gene regulation, Nat. Rev. Mol. Cell Biol. **24**, 288 (2023).

[6] P. Li, S. Banjade, H.-C. Cheng, S. Kim, B. Chen, L. Guo, M. Llaguno, J. V. Hollingsworth, D. S. King, S. F. Banani, *et al.*, Phase transitions in the assembly of multivalent signalling proteins, Nature **483**, 336 (2012).

[7] H. Wu, Higher-order assemblies in a new paradigm of signal transduction, Cell **153**, 287 (2013).

[8] X. Su, J. A. Ditlev, E. Hui, W. Xing, S. Banjade, J. Okrut, D. S. King, J. Taunton, M. K. Rosen, and R. D. Vale, Phase separation of signaling molecules promotes T cell receptor signal transduction, Science **352**, 595 (2016).

[9] A. Molliex, J. Temirov, J. Lee, M. Coughlin, A. P. Kanagaraj, H. J. Kim, T. Mittag, and J. P. Taylor, Phase separation by low complexity domains promotes stress granule assembly and drives pathological fibrillization, Cell **163**, 123 (2015).

[10] A. Patel, H. O. Lee, L. Jawerth, S. Maharana, M. Jahnel, M. Y. Hein, S. Stoynov, J. Mahamid, S. Saha, T. M. Franzmann, A. Pozniakovski, I. Poser, N. Maghelli, L. A. Royer, M. Weigert, E. W. Myers, S. Grill, D. Drechsel, A. A. Hyman, and S. Alberti, A liquid-to-solid phase transition of the ALS protein FUS accelerated by disease mutation, Cell **162**, 1066 (2015).

[11] G. Gaglia, R. Rashid, C. Yapp, G. N. Joshi, C. G. Li, S. L. Lindquist, K. A. Sarosiek, L. Whitesell, P. K. Sorger, and S. Santagata, HSF1 phase transition mediates stress adaptation and cell fate decisions, Nat. Cell Biol. **22**, 151 (2020).

[12] S. Wegmann, B. Eftekharzadeh, K. Tepper, K. M. Zoltowska, R. E. Bennett, S. Dujardin, P. R. Laskowski, D. MacKenzie, T. Kamath, C. Commins, C. Vanderburg, A. D. Roe, Z. Fan, A. M. Molliex, A. Hernandez-Vega, D. Muller, A. A. Hyman, E. Mandelkow, J. P. Taylor, and B. T. Hyman, Tau protein liquid–liquid phase separation can initiate tau aggregation, EMBO J. **37**, e98049 (2018).

[13] S. Alberti and A. A. Hyman, Biomolecular condensates at the nexus of cellular stress, protein aggregation disease and ageing, Nat. Rev. Mol. Cell Biol. **22**, 196 (2021).

[14] J. Nam and Y. Gwon, Neuronal biomolecular condensates and their implications in neurodegenerative diseases, Front. Aging Neurosci. **15**, 1145420 (2023).

[15] S. Spannl, M. Tereshchenko, G. J. Mastromarco, S. J. Ihn, and H. O. Lee, Biomolecular condensates in neurodegeneration and cancer, Traffic **20**, 890 (2019).

[16] A. Boija, I. A. Klein, and R. A. Young, Biomolecular condensates and cancer, Cancer Cell **39**, 174 (2021).

[17] K. Taniue and N. Akimitsu, Aberrant phase separation and cancer, FEBS J. **289**, 17 (2022).

[18] X. Tong, R. Tang, J. Xu, W. Wang, Y. Zhao, X. Yu, and S. Shi, Liquid–liquid phase separation in tumor biology, Signal Transduct. Target. Ther. **7**, 221 (2022).

[19] C. P. Brangwynne, C. R. Eckmann, D. S. Courson, A. Rybarska, C. Hoege, J. Gharakhani, F. Jülicher, and A. A. Hyman, Germline P granules are liquid droplets that localize by controlled dissolution/condensation, Science **324**, 1729 (2009).

[20] S. An, R. Kumar, E. D. Sheets, and S. J. Benkovic, Reversible compartmentalization of de novo purine biosynthetic complexes in living cells, Science **320**, 103 (2008).

[21] A. M. Pedley, J. P. Boylan, C. Y. Chan, E. L. Kennedy, M. Kyoung, and S. J. Benkovic, Purine biosynthetic enzymes assemble into liquid-like condensates dependent on the activity of chaperone protein HSP90, J. Biol. Chem. **298**, 101845 (2022).

[22] M. Prouteau and R. Loewith, Regulation of cellular metabolism through phase separation of enzymes, Biomolecules **8**, 160 (2018).

[23] H. Wang, F. M. Kelley, D. Milovanovic, B. S. Schuster, and Z. Shi, Surface tension and viscosity of protein condensates quantified by micropipette aspiration, Biophys. Rep. **1**, 100011 (2021).

[24] I. Lifshitz and V. Slyozov, The kinetics of precipitation from supersaturated solid solutions, J. Phys. Chem. Solid **19**, 35 (1961).

[25] C. Wagner, Theorie der alterung von niederschlägen durch umlösen (ostwald-reifung), Zeitschrift Für Elektrochemie Berichte Der Bunsengesellschaft Für Phys. Chemie **65**, 581 (1961).

[26] M.-M. Poo and R. A. Cone, Lateral diffusion of rhodopsin in necturus rods, Exp. Eye Res. **17**, 503 (1973).

[27] P. Liebman and G. Entine, Lateral diffusion of visual pigment in photoreceptor disk membranes, Science **185**, 457 (1974).

[28] J. Lippincott-Schwartz, E. Snapp, and A. Kenworthy, Studying protein dynamics in living cells, Nat. Rev. Mol. Cell Biol. **2**, 444 (2001).

[29] F. Pincet, V. Adrien, R. Yang, J. Delacotte, J. E. Rothman, W. Urbach, and D. Tareste, FRAP to characterize molecular diffusion and interaction in various membrane environments, PLOS ONE **11**, 1 (2016).

[30] K. A. Burke, A. M. Janke, C. L. Rhine, and N. L. Fawzi, Residue-by-residue view of *in vitro* FUS granules that bind the C-terminal domain of RNA polymerase II, Mol. Cell **60**, 231 (2015).

[31] S. F. Banani, A. M. Rice, W. B. Peeples, Y. Lin, S. Jain, R. Parker, and M. K. Rosen, Compositional control of phase-separated cellular bodies, Cell **166**, 651 (2016).

[32] S. Jain, J. R. Wheeler, R. W. Walters, A. Agrawal, A. Barsic, and R. Parker, ATPase-modulated stress granules contain a diverse proteome and substructure, Cell **164**, 487 (2016).

[33] W. M. J. Aumiller, F. Pir Cakmak, B. W. Davis, and C. D. Keating, RNA-based coacervates as a model for membraneless organelles: Formation, properties, and interfacial liposome assembly, Langmuir **32**, 10042 (2016).

[34] N. O. Taylor, M.-T. Wei, H. A. Stone, and C. P. Brangwynne, Quantifying dynamics in phase-separated condensates using fluorescence recovery after photobleaching, Biophys. J. **117**, 1285 (2019).

[35] L. Hubatsch, L. M. Jawerth, C. Love, J. Bauermann, T. D. Tang, S. Bo, A. A. Hyman, and C. A. Weber, Quantitative theory for the diffusive dynamics of liquid condensates, eLife **10**, e68620 (2021).

[36] S. Bo, L. Hubatsch, J. Bauermann, C. A. Weber, and F. Jülicher, Stochastic dynamics of single molecules across phase boundaries, Phys. Rev. Res. **3**, 043150 (2021).

[37] F. Muzzopappa, J. Hummert, M. Anfossi, S. A. Tashev, D.-P. Herten, and F. Erdel, Detecting and quantifying liquid–liquid phase separation in living cells by model-free calibrated half-bleaching, Nat. Commun. **13**, 7787 (2022).

[38] A. W. Folkmann, A. Putnam, C. F. Lee, and G. Seydoux, Regulation of biomolecular condensates by interfacial protein clusters, Science **373**, 1218 (2021).

[39] C. F. Lee, Scaling law and universal drop size distribution of coarsening in conversion-limited phase separation, Phys. Rev. Res. **3**, 043081 (2021).

[40] H. T. Nguyen, N. Hori, and D. Thirumalai, Condensates in RNA repeat sequences are heterogeneously organized and exhibit reptation dynamics, Nat. Chem. **14**, 775 (2022).

[41] Y. Zhang, A. G. Pyo, R. Kliegman, Y. Jiang, C. P. Brangwynne, H. A. Stone, and N. S. Wingreen, The exchange dynamics of biomolecular condensates, eLife **12**, RP91680 (2024).

[42] L. Hubatsch, S. Bo, T. S. Harmon, A. A. Hyman, C. A. Weber, and F. Jülicher, Transport kinetics across interfaces between coexisting liquid phases, bioRxiv 10.1101/2024.12.20.629798 (2025).

[43] J. Wang, J.-M. Choi, A. S. Holehouse, H. O. Lee, X. Zhang, M. Jahnel, S. Maharana, R. Lemaitre, A. Pozniakovsky, D. Drechsel, I. Poser, R. V. Pappu, S. Alberti, and A. A. Hyman, A molecular grammar governing the driving forces for phase separation of prion-like RNA binding proteins, Cell **174**, 688 (2018).

[44] G. M. Ginell and A. S. Holehouse, An introduction to the stickers-and-spacers framework as applied to biomolecular condensates, in *Phase-Separated Biomolecular Condensates: Methods and Protocols*, edited by H.-X. Zhou, J.-H. Spille, and P. R. Banerjee (Springer US, New York, NY, 2023) pp. 95–116.

[45] J.-M. Choi, A. S. Holehouse, and R. V. Pappu, Physical principles underlying the complex biology of intracellular phase transitions, Annu. Rev. Biophys. **49**, 107 (2020).

[46] T. Mittag and R. V. Pappu, A conceptual framework for understanding phase separation and addressing open questions and challenges, Mol. Cell **82**, 2201 (2022).

[47] Z. Shen, B. Jia, Y. Xu, J. Wessén, T. Pal, H. S. Chan, S. Du, and M. Zhang, Biological condensates form percolated networks with molecular motion properties distinctly different from dilute solutions, eLife **12**, e81907 (2023).

[48] T. Wu, M. R. King, Y. Qiu, M. Farag, R. V. Pappu, and M. D. Lew, Single-fluorogen imaging reveals distinct environmental and structural features of biomolecular condensates, Nat. Phys. , 1 (2025).

[49] See Supplemental Material at [URL-will-be-inserted-by-publisher] for details.

[50] J. W. Cahn and J. E. Hilliard, Free energy of a nonuniform system. I. interfacial free energy, J. Chem. Phys. **28**, 258 (1958).

[51] R. Skeel and M. Berzins, A method for the spatial discretization of parabolic equations in one space variable, Siam J. Sci. Stat. Comput. **11** (1990).

[52] P. M. McCall, K. Kim, M. Ruer-Gruß, J. Peychl, J. Guck, A. A. Hyman, and J. Brugués, Label-free composition determination for biomolecular condensates with an arbitrarily large number of components, bioRxiv 10.1101/2020.10.25.352823 (2023).

[53] L. Jawerth, E. Fischer-Friedrich, S. Saha, J. Wang, T. Franzmann, X. Zhang, J. Sachweh, M. Ruer, M. Ijavi, S. Saha, J. Mahamid, A. A. Hyman, and F. Jülicher, Protein condensates as aging maxwell fluids, Science **370**, 1317 (2020).

[54] S. Biffi, R. Cerbino, F. Bomboi, E. M. Paraboschi, R. Asselta, F. Sciortino, and T. Bellini, Phase behavior and critical activated dynamics of limited-valence DNA nanostars, Proc. Natl. Acad. Sci. **110**, 15633 (2013).

[55] Y. Sato, T. Sakamoto, and M. Takinoue, Sequence-based engineering of dynamic functions of micrometer-sized DNA droplets, Sci. Adv. **6**, eaba3471 (2020).

[56] B.-j. Jeon, D. T. Nguyen, G. R. Abraham, N. Conrad, D. K. Fygenson, and O. A. Saleh, Salt-dependent properties of a coacervate-like, self-assembled DNA liquid, Soft Matter **14**, 7009 (2018).

[57] S. Agarwal, D. Osmanovic, M. Dizani, M. A. Klocke, and E. Franco, Dynamic control of DNA condensation, Nat. Commun. **15**, 1915 (2024).

[58] E. Kengmana, E. Ornelas-Gatdula, K.-L. Chen, and R. Schulman, Spatial control over reactions via localized transcription within membraneless DNA nanostar droplets, J. Am. Chem. Soc. **146**, 32942 (2024).

[59] K. Skipper and S. Wickham, Core-shell coacervates formed from DNA nanostars, ChemRxiv 10.26434/chemrxiv-2024-07pvd (2024).

[60] D. T. Nguyen, B.-j. Jeon, G. R. Abraham, and O. A. Saleh, Length-dependence and spatial structure of DNA partitioning into a DNA liquid, Langmuir **35**, 14849 (2019).

[61] D. Y. Zhang and E. Winfree, Control of DNA strand displacement kinetics using toehold exchange, J. Am. Chem. Soc. **131**, 17303 (2009).

[62] S. Do, C. Lee, T. Lee, D.-N. Kim, and Y. Shin, Engineering DNA-based synthetic condensates with programmable material properties, compositions, and functionalities, Sci. Adv. **8**, eabj1771 (2022).

[63] S. Kent, K. Brown, C.-h. Yang, N. Alsaihati, C. Tian, H. Wang, and X. Ren, Phase-separated transcriptional condensates accelerate target-search process revealed by live-cell single-molecule imaging, Cell Rep. **33**, 108248 (2020).

[64] S. Hao, Y. J. Lee, N. B. Goldfajn, E. Flores, J. Liang, H. Fuehrer, J. Demmerle, J. Lippincott-Schwartz, Z. Liu, S. Sukenik, *et al.*, YAP condensates are highly organized hubs, iScience **27**, 109927 (2024).

[65] M.-T. Wei, S. Elbaum-Garfinkle, A. S. Holehouse, C. C.-H. Chen, M. Feric, C. B. Arnold, R. D. Priestley, R. V. Pappu, and C. P. Brangwynne, Phase behaviour of disordered proteins underlying low density and high permeability of liquid organelles, Nat. Chem. **9**, 1118 (2017).

[66] N. Galvanetto, M. T. Ivanović, A. Chowdhury, A. Sottini, M. F. Nüesch, D. Nettels, R. B. Best, and B. Schuler, Extreme dynamics in a biomolecular condensate, Nature **619**, 876 (2023).

[67] V. Grigorev, N. S. Wingreen, and Y. Zhang, Conformational entropy of intrinsically disordered proteins bars intruders from biomolecular condensates, PRX Life **3**, 013011 (2025).

[68] B. Wang, L. Zhang, T. Dai, Z. Qin, H. Lu, L. Zhang, and F. Zhou, Liquid–liquid phase separation in human health and diseases, Signal Transduct. Target. Ther. **6**, 290 (2021).

[69] D. M. Mitrea, M. Mittasch, B. F. Gomes, I. A. Klein, and M. A. Murcko, Modulating biomolecular condensates: a novel approach to drug discovery, Nat. Rev. Drug Discov. **21**, 841 (2022).